González, M., Crespo, M., Baselga, J. y Pozuelo, J. (2016): Carbon nanotube scaffolds with controlled porosity as electromagnetic absorbing materials in the gigahertz range. *Nanoscale*, 8 (20), pp. 10724-10730.

DOI: 10.1039/c6nr02133f

Carbon nanotube scaffolds with controlled porosity as electromagnetic absorbing materials in the gigahertz range^

M. González,[a] M. Crespo,[a,b] J. Baselga[a] and J. Pozuelo*[a]

Control of the microscopic structure of CNT nanocomposites allows modulation of the electromagnetic shielding in the gigahertz range. The porosity of CNT scaffolds has been controlled by two freezing proto-cols and a subsequent lyophilization step: fast freezing in liquid nitrogen and slow freezing at −20 °C. Mercury porosimetry shows that slowly frozen specimens present a more open pore size (100–150 μm) with a narrow distribution whereas specimens frozen rapidly show a smaller pore size and a hetero-geneous distribution. 3D-scaffolds containing 3, 4, 6 and 7% CNT were infiltrated with epoxy and speci-mens with 2, 5 and 8 mm thicknesses were characterized in the GHz range. Samples with the highest pore size and porosity presented the lowest reflected power (about 30%) and the highest absorbed power (about 70%), which allows considering them as electromagnetic radiation absorbing materials.

Introduction

Electromagnetic interference (EMI) is a disturbance that affects electrical circuits due to the electromagnetic radiation emitted by other electronic devices. This disturbance may interrupt, obstruct, or otherwise degrade the performance of the circuit. Nowadays, the extensive development of new telecommunication devices and new electronic equipment in the GHz range has elevated the electromagnetic pollution to very high levels, justifying the need to find materials able to shield unintended electromagnetic radiation.[1,2] Several studies have been conducted to reach efficient EMI shielding materials.[3–5]

Electromagnetic shields can block the transmission of radiation through three commonly accepted mechanisms: reflection, absorption and multiple reflections.[6] According to Schelkunoff's theory[7] multiple reflections can be neglected when the thickness of the slab is greater than the skin depth (δ),[8–11] which is the depth at which the incident field decreases at $1/e$ of its initial value. When electromagnetic radiation of a given power reaches a material, one part is reflected, another portion is transmitted through the material and the difference between them is regarded as the absorbed radiation. The power of the reflected wave is related to the impedance mismatch at the plane of incidence, or at the interface between the propagating medium and the material. Nowadays protection of electronic devices from external radiation may be performed by the reflection of the incident wave, or by a process of absorption–dissipation.[6] For applications with high reflection requirements (antennas), high impedance mismatch is satisfied through the use of metallic materials. When low reflection is needed, it is necessary to achieve the minimum impedance mismatch. For this purpose, the use of heterogeneous conductive materials with open, highly porous structures becomes an interesting field of research. In these systems, the impedance mismatch is significantly lower than that in homogeneous and compact materials, and therefore the power of the reflected wave is also smaller.[12]

Both the reflected and absorbed powers are closely related to the electrical conductivity of the material. Homogeneous conductors show high reflection losses, causing only a small portion of the incident radiation to enter and propagate through the material. However, good electrical conductors with low impedance mismatch can overcome this limitation, and, if combined with other requirements such as lightweight, flexibility and minimum cost, may constitute a breakthrough with a broad range of applications in flexible electronics, aerospace or automobile manufacturing.[13]

In this context, low density polymer composites incorporating conductive carbonaceous inclusions are considered as promising materials for absorbing electromagnetic radiation.[14]

[a]*Departamento de Ciencia e Ingeniería de Materiales e Ingeniería Química (IAAB), Universidad Carlos III de Madrid, 28911 Leganés, Madrid, Spain. E-mail: jpozue@ing.uc3m.es; Fax: +34 91 6249430*

[b]*School of Engineering and Materials Science, Queen Mary, University of London, 327 Mile End Road, London, UK*

^Electronic supplementary information (ESI) available: Scheme of hydrogenated derivative of diglycidyl ether of bisphenol-A (HDGEBA) and *m*-xylylenediamine; X-ray diffractograms of pristine CNT and oxidized CNT; glass transition temp-eratures of composites; electromagnetic shielding analysis in the 1–18 GHz fre-quency range.

It has been demonstrated[14–19] that their shielding efficiency (SE) is enhanced when the filler electrical conductivity, aspect ratio or content are increased.[20] For example, it has been shown that values of SE around 20 dB are reached with 15 wt% of carbon black, 5–10 wt% carbon nanofibers.[9] However, in most reported polymer-based nanocomposites, SE over 20 dB has been only reached with high filler loadings,[26] a fact that is neither economically desirable nor viable for processing.

Low density carbon nanotube sponges (0.02 g cm^{-3}) are an alternative approach that has been recently reported.[10] These new materials are prepared by chemical vapour deposition with a pore size in the range of 1 micron. They present an extremely high specific SE, around 1100 dB cm^3 g^{-1} but their very high electrical conductivity enhances the reflective component making them useful in layered structures and not as stand-alone materials.

Graphene is another alternative conductive material. The SE of a single graphene monolayer has been measured yielding a value as high as 2.27 dB, which corresponds to seven times the SE of gold.[25] This fact along with its potential high conductivity and surface area, allows adding chemically derived graphene to the list of carbon nanofillers for EMI shielding applications.[21–24]

To address the problem of the impedance mismatch when using highly conductive carbonaceous nanoparticles it seems necessary to focus on their microscopic organization looking for producing a highly porous outer surface with a pore size similar to the wavelength of the incident radiation. In principle, when radiation impinges on the surface of a porous conductive material, it gets distributed among the pores and their walls. The major portion of the reflected radiation will arise from reflections with the pore walls, reflections from the inner part of the pores being a much smaller contribution. Therefore, the fraction and size of the pores created on the surface of a conductive compound may be good tools for modulating the phenomenon of reflection of electromagnetic radiation. If the process of reflection of radiation is decreased, a larger fraction of the radiation will penetrate into the material being possible to remove it by another mechanism (absorption). For this reason, an exhaustive control of porosity in composite conductors may be the way to obtain electromagnetic radiation absorbing materials.[27]

In this work, we have controlled the porosity of scaffolds by controlling the freezing rate of aqueous dispersions of carbon nanotubes and subsequent lyophilisation. For this purpose, two processes were used: "fast freezing" in liquid nitrogen and "slow freezing" at −20 °C. In our "fast freezing" methodology, there is a huge ice-nucleation rate, which causes the formation of small ice crystals, while through the "slow freezing" process the nucleation rate is lower and as a result the size of ice crystals is increased; the subsequent lyophilisation sublimates ice crystals fixing the pore size. Furthermore, ice crystal growth displaces carbon nanotubes to the intercrystalline regions compressing them and forming the pore walls; as it is shown, differences in the crystal volume will change the CNT connectivity within the pore walls and, consequently, the conductivity of the material. Polymer based porous composites were obtained by infiltration of 3D-scaffolds containing 3, 4, 6 and 7 wt% CNT with an epoxy resin. Cured samples were machined to the final geometry required for characterization.

Experimental

Materials

Chitosan was supplied by Sigma-Aldrich. The hydrogenated derivative of diglycidyl ether of bisphenol-A (HDGEBA) epoxy resin was supplied by CVC Specialty Chemicals (USA); its epoxy equivalent mass (210 g mol^{-1}) was determined by acid titration. *m*-Xylylenediamine (Sigma-Aldrich) was used as a curing agent. Multi-walled carbon nanotubes Graphistrength® C100 (with a purity >90 wt%) were purchased from Arkema Inc. To remove the extreme CNT hydrophobicity, surface functionalization with polar groups[28] was performed using the H_2O_2/UV method which gives a higher aspect ratio than other oxidizing procedures.[29–32] In a typical experiment 1 g of CNT was treated with 100 mL of H_2O_2 in an ultrasonic bath for three minutes; afterwards, the dispersion was stirred and exposed to UV light (Philips Lighting 250HPLN 250W) for 15 minutes,[32] filtered, washed with distilled water until neutral pH and dried under vacuum.

CNT scaffold preparation

Four oxidized CNT-water dispersions were prepared by sonicating appropriate amounts of CNT (3, 4, 6, 7 wt%) in 15 mL of aqueous 0.15 M acetic acid in an ultrasonic bath for 30 min; chitosan (1 wt%) was then added and the mixture was stirred mechanically for 24 hours. In acidic medium, protonated chitosan amino groups interact with the acid groups of oxidized CNT acting thus as a binder for CNT.

Dispersions were frozen at two different rates to control the pore size: (i) slow freezing in a freezer at −20 °C, and (ii) fast freezing by immersing in liquid nitrogen. After freezing, the scaffolds were lyophilized to fix the porous structure, and treated with glutaraldehyde vapours for 24 hours to crosslink chitosan residues. Glutaraldehyde reacts with the free amino groups of the chitosan enhancing the strength of the scaffold which is needed to withstand the subsequent infiltration process.

A stoichiometric mixture of HDGEBA and the curing agent *m*-xylylenediamine (MXD) (see the ESI†) was used to infiltrate the scaffolds under vacuum. Vacuum was necessary to ensure that all air cavities and pores were completely filled with the epoxy mixture. Infiltrated scaffolds were cured in an oven for one hour at 90 °C and post-cured for another hour at 120 °C.

Techniques

Oxidized CNTs were characterized by wide-angle X-Ray Diffraction (XRD, Panalytical X'pert Pro X-ray diffractometer) with Cu Kα radiation (λ = 0.15406 nm). Differential scanning calorimetry (Mettler Toledo DSC 822e) was used to measure the T_g of the epoxy resin. SEM images of the scaffolds were obtained

with a Philips XL 30 scanning electron microscope. Mercury porosimetry was carried out using Poremaster Series Quantachrome Instruments: Hg surface tension of 480 kJ m^{-2}, Hg contact angle of 1400. Pressure range: 1.372 kPa to 345.275 kPa. Electrical properties of the composites were evaluated using a HP 34401A device with 100 μΩ resolution and 10 GΩ upper limit; measurements were performed in a 4-wire DC configuration to obviate the electrical resistance of the wires.

The global electromagnetic shielding efficiency, SE_T, can be quantified as the sum of the contributions of reflection and absorption mechanisms. For these purposes, the scattering parameters S_{11} and S_{21} were determined using a vector network analyzer (Agilent, ENA, E5071) with a 7 mm coaxial transmission line adapter in the range of 1 to 18 GHz. An ENA instrument measures both the transmitted coefficient $T = P_T/P_I$ and reflected coefficient $R = P_R/P_I$, therefore the absorbed coefficient by the material is:[33]

$$A = 1 - (R + T)$$

The ratios between the scattering parameters and the transmission, reflection and absorption EMI shielding effectiveness are given by equations.

$$SE_T = -10\log T = -10\log\left(|S_{21}|^2\right)$$
$$SE_R = -10\log(1-R) = -10\log\left(1-|S_{11}|^2\right)$$
$$SE_A = -10\log[T/(1-R)] = -10\log\left[|S_{21}|^2/\left(1-|S_{11}|^2\right)\right]$$

The scattering parameters were also used to calculate the complex magnetic permeability and dielectric permittivity of the CNT scaffolds. The measurements were performed according to the transmission/reflection method.[34] Cured samples were machined to the final required geometry for the coaxial line: rectangular toroids of nominal internal and external diameters close to 3.04 and 7 mm respectively. Using the built-in software, a geometry correction was applied for small deviations from nominal geometry.[34]

Results and discussion

Structural characterization of scaffolds

X-ray diffraction was used to confirm that the oxidized carbon nanotubes maintain the crystal structure of the original CNT. The diffraction pattern of the oxidized carbon nanotubes (see the ESI†) shows two intense peaks at scattering angles of 26.1° and 44.25° which correspond to (002) and (101) planes of hexagonal graphite respectively. Some low intensity peaks can also be observed which correspond to iron oxides due to the remaining catalyst used for its synthesis. The peaks that appear at scattering angles of 35° and 64° correspond to 311 and 400 planes of ferrite and the amorphous peak at 44 corresponds to the 311 plane of Fe_3C.

Fig. 1 shows SEM micrographs of low and fast freezing for systems with 3 and 6 wt% of carbon nanotubes as representative examples. The big difference in pore size with freezing rate can be clearly observed; sizes are in the order of 100–150 μm

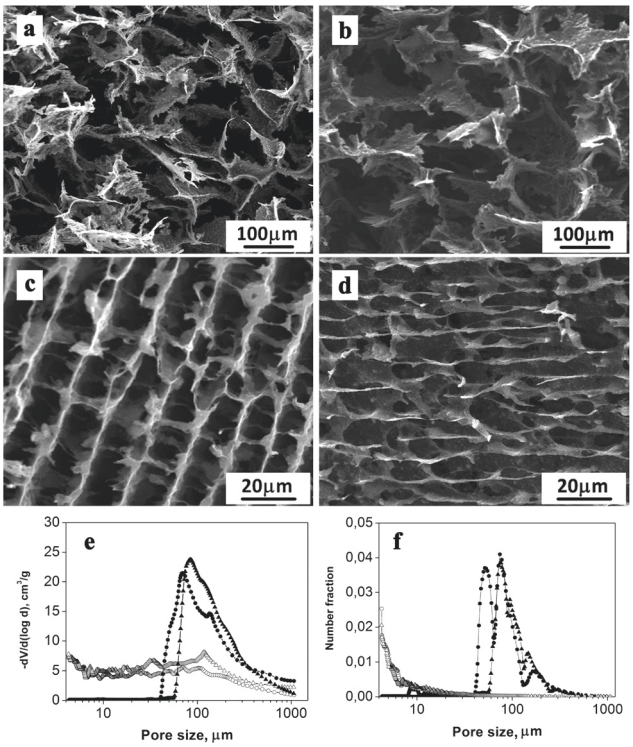

Fig. 1 SEM micrographs of (a) CNT3% – slow, (b) CNT6% – slow, (c) CNT3% – fast, (d) CNT6% – fast, (scale bars correspond to 100 μm for slow freezing and to 20 μm for fast freezing), (e, f) pore size distributions by mercury porosimetry: CNT3% – fast (○), CNT6% – fast (△), CNT3% – slow (●),CNT6% – slow (▲).

when cooled at −20 °C and around 20 μm when cooled at liquid nitrogen temperature. This result can be qualitatively explained in terms of nucleation theory since both freezing methods differ in the undercooling extent. High undercooling should form a big number of embryos with a small size that will remain small after the growth process is finished; the opposite should hold for the low undercooling process. Since the embryo size, r_c, scales with undercooling as $r_c \propto (\Delta T)^{-1}$, the ratio of embryo sizes for the slow and fast processes, $r_{c,S}/r_{c,F}$, should be given by the reciprocal ratio of their corresponding undercooling, which is around 10; this value is in fair enough coincidence with the observed pore size ratios as measured by mercury porosimetry (see Table 1), which is around 5–7. The slight dependence of pore size on the CNT concentration for the slowly frozen samples may be attributed to the aggregation state of CNT in the initial aqueous dispersions, which should be higher for the more concentrated systems.

The average pore size obtained by porosimetry confirms data from image analysis as well as the closely related data on the surface area. Nevertheless, one should be aware that mercury porosimetry does not actually measure the internal pore size, but it rather determines the largest connection (throat or pore channel) from the sample surface towards that pore.[35] For this reason the porosity obtained for fast frozen

Table 1 Mercury porosimetry analysis of scaffolds with CNT compositions in the range of 3–7%

	Slow freezing				Fast freezing			
CNT content	3%	4%	6%	7%	3%	4%	6%	7%
Mean pore, μm	105	112	127	141	19	15	21	21
Surface area, $m^2\ g^{-1}$	0.52	0.49	0.41	0.37	2.01	2.15	2.27	2.18
Porosity, %	63	58	56	61	31	21	34	41
Density, mg cm^{-3}	46	40	44	47	33	47	38	52
Tortuosity	1.52	1.55	1.59	1.54	1.88	1.89	1.84	1.84
K_t, $nm^2 \times 10^{-3}$	28.6	27.7	35.4	49.9	0.36	0.15	0.52	0.12
Throat/pore ratio	0.23	0.28	0.30	0.31	0.38	0.35	0.32	0.42

samples is different and lower than for the slowly frozen ones although similar values should be expected since the starting dispersions are the same and no significant volume changes were detected after freezing. The anisotropy in the formation of pores with nitrogen freezing can be observed when analysing tortuosity. The tortuosity in fast freezing systems is greater than in systems prepared through slow freezing. It might be speculated that this is due to the greater heterogeneity of the pores created with the fast freezing, although the tortuosity is highly dependent on the pore size, throat or pore channel, *etc*.[35] As expected, the permeability (K_t) of mercury was significantly higher in slow freezing systems, but slight differences were observed in the throat/pore ratio values. These results suggest that there are no major differences in the connectivity of the pores, just in the pore sizes.

DSC analysis showed that infiltration with HDGEBA: *m*-xylylenediamine did not affect the thermal properties of the matrix. The glass transition temperatures of these systems are shown in Table S1 of the ESI.†

DC electrical conductivity

Table 2 shows the DC electrical conductivity of the CNT composites. The high values of conductivity, even for the lowest CNT concentrations, indicate that even at low loads, systems are beyond the percolation threshold. This is a general result[36] that is usually attributed to the local compression that CNTs undergo within the pore walls as ice crystals form during the freezing process, which is indeed the key aspect for reaching lower percolation thresholds through segregated conductive networks. CNTs thus form a non-interrupted conductive network through the whole length of the composite. However, the cellular nature of the conductive network does affect the conductivity since scaffolds prepared by fast freezing show slightly higher conductivity values than their slowly frozen analogues. This fact can be easily explained considering the surface area of the pores; small pore systems present a higher surface area thus providing more percolation paths for the conduction process.

Table 2 DC conductivity of scaffolds with the content of CNT in the range of 3–7%

	σ, S m^{-1}	
CNT content, wt%	Slow freezing	Fast freezing
3	10.3	12
4	12.3	14.4
6	13.6	16.6
7	14.1	16.6

Electromagnetic shielding

Three mechanisms for electromagnetic shielding are commonly accepted: reflection, absorption and multiple reflections.[6] Multiple reflections are produced by the coupling of the reflected radiation on the first incidence plane and reflection in the final plane of the material. This radiation coupling originates constructive and destructive wave interferences that have frequency dependence. According to Schelkunoff's theory[7] this term can be neglected when the thickness of the material is considerably higher than the conductor skin depth (δ),[9,11] which is the depth at which the incident field decreases at $1/e$ of its initial value.[8]

Fig. 2 shows the calculated skin depth for all our samples as a function of frequency. We estimate that in samples with a slab thickness higher than twice the value of the skin depth, multiple reflections may become negligible. Therefore, only data above 8 GHz have been selected for the discussion on shielding mechanisms.

Fig. 3 shows the relative complex permittivity of composites. The real and imaginary components represent respectively the storage and loss of the electromagnetic energy, and can be assessed as dielectric interactions between the electromagnetic field and the shielding material. It is noteworthy that enhanced polarization processes have been widely observed in highly loaded CNT–polymer composites (~15–20 wt%) because in such systems there is a high number of interfaces and grain boundaries that contribute to space charge polarization.[37] The freeze drying process used in our material causes the concentration of carbon nanotubes in the walls of the scaffold to be much greater than in a homogeneous dispersion. Consequently, freeze drying increases the CNT connectivity at the walls.

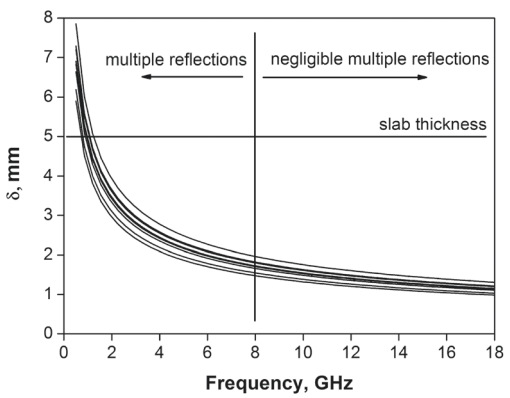

Fig. 2 Skin depth as a function of frequency. Multiple reflection limits on the scaffold slab.

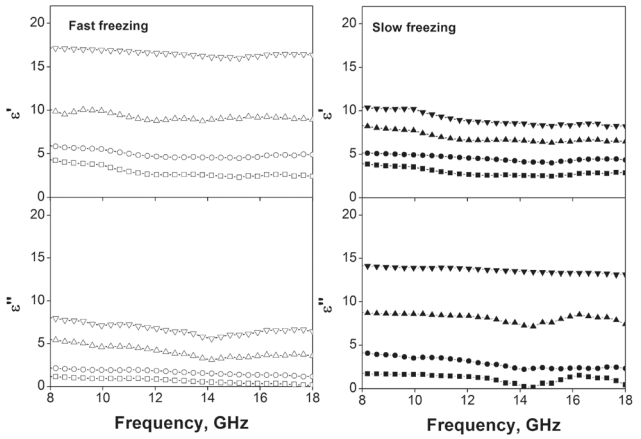

Fig. 3 Dielectric permittivity of scaffolds with CNT percentages of 3% (squares), 4% (circles), 6% (triangles), 7% (down triangles).

According to the effective medium theory, the permittivity of the material will have the contribution of both, epoxy and CNTs, and hence, its value will be lower than that of a material exhibiting analogous conductivity values but being compact or non-porous.[38] According to Hrubesh *et al.* these structures might exhibit low dielectric properties, which can be more accurately described rather by an epoxy-like behaviour than by a conductor-like one and will depend strongly on the volume fraction of the conductor phase.[39] It has been corroborated that the effective permittivity of aerogels, with almost all phase combinations, geometries and distributions, is circumscribed between the Wiener bounds, which are less restrictive and depend on the volume fraction and the complex permittivity of each phase in the composite. It is hence clear that for materials containing high volume fractions of epoxy, the permittivity of the composite should be smaller than that due to the conductive filler.[40,41]

Fig. 4 shows the reflected, absorbed and transmitted power for 4% and 6% CNT compositions as an example (powers throughout the frequency range are presented in the ESI†). In all cases the transmitted power is particularly low, not exceeding in any case 10% of incident power. In all cases, the absorbed power is significantly greater than the power reflected by the material. These results allow us to conclude that all the prepared materials can be considered as electromagnetic radiation absorbing materials.

Comparing the reflected power of fast and slow frozen systems, it can be observed that the latter presents considerably lower values than the former for all the studied concentrations. We attribute this behaviour to the effect of the pore size and porosity, which is higher when samples are frozen slowly. Zhao *et al.*[12] studied the shielding behaviour of carbon fibre epoxy composites by varying the thickness of the fibres and the size of the grid; the authors observed that when the ratio grid size/thickness of fibre increased, the reflection of electromagnetic radiation decreased. This observation is in

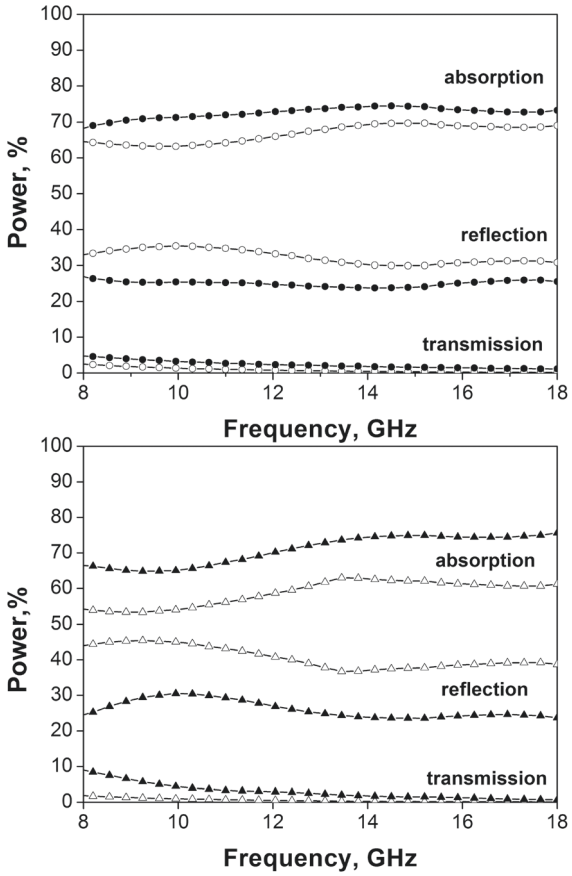

Fig. 4 Reflected, absorbed and transmitted powers in the frequency range of 8–18 GHz with CNT compositions of 4 and 6%. CNT4% – slow (●), CNT4% – fast (○), CNT6% – slow (▲), CNT6% – fast (△). Composite thickness: 5 mm.

agreement with our results. An increase in the ratio between the pore size and the size of the conductive wall should cause a lower impedance mismatch between the air and the absorbing material. In qualitative terms, a measure of this parameter is given by the porosity (see Table 1) of the samples. Thus, samples with more porosity present a lower impedance mismatch and more radiation is therefore able to penetrate into the material for absorption.

The electromagnetic shielding mechanism was evaluated by the shielding efficiency (SE) analysis. Fig. 5 shows the SE in transmission for scaffold composites over 8 to 18 GHz (results for the complete frequency range are presented in the ESI†). It can be observed that SE increases by increasing the amount of CNT in the composites mainly due to their higher electrical conductivity. Concerning the frequency dependence, CNT composites can be represented as a random set of interconnected conductors with dielectric interfacial junctions. These interfaces generate capacitors that restrict current to flow only through resistive paths. As capacitive reactance is inversely proportional to frequency when the frequency increases, the impedance associated with the capacitive element decreases; the bulk material offers thus less resistance to electric charge

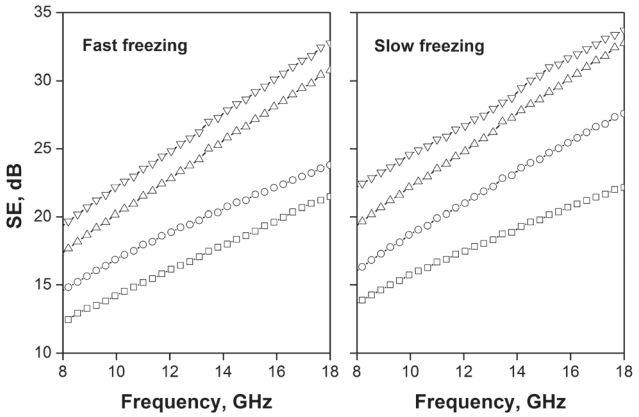

Fig. 5 Electromagnetic efficiency in the frequency range of 8–18 GHz with CNT percentages of: 3% (□), 4% (○), 6% (△), 7% (▽). Composite thickness: 5 mm.

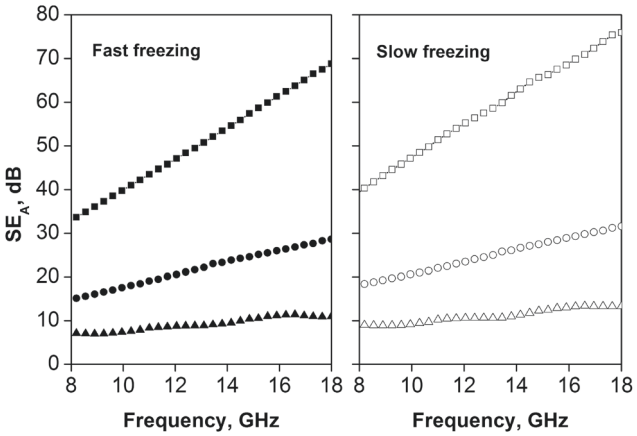

Fig. 7 Absorption electromagnetic efficiency of scaffolds with 6% CNT in the frequency range of 8–18 GHz. Composite thickness: 2 mm (triangles), 5 mm (circles), and 8 mm (squares).

transmission. For this reason the electromagnetic shielding increases with the frequency.

Fig. 6 shows the SE due to reflection, absorption and transmission for the scaffold composites with 4 and 6 wt% CNT, over 8 to 18 GHz. In all cases, reflection losses are very small in comparison with absorption. Low reflection losses could be attributed to the highly porous structure of the scaffolds which have impedances comparable to that of the propagating medium that enable the penetration of the incident wave into the composite for its dissipation. Consequently, absorption is found to be the foremost energy loss mechanism and increases with frequency. As for the total shielding efficiency, it is also found that SE_A increases with increasing CNT content.

According to Al-Saleh *et al.*,[8] electromagnetic efficiency due to the absorption process is proportional to the material thickness. Fig. 7 shows a comparative study of SEA of CNT 6% for three different thickness values: 2, 5 and 8 mm, in scaffold composites obtained by fast and slow freezing. As expected, the efficiency of electromagnetic shielding in the process of absorption was proportional to the thickness of the scaffold and also to the frequency. These results allow us to estimate the necessary thickness of a coating made by these methods to achieve optimal electromagnetic shielding for a specific application.

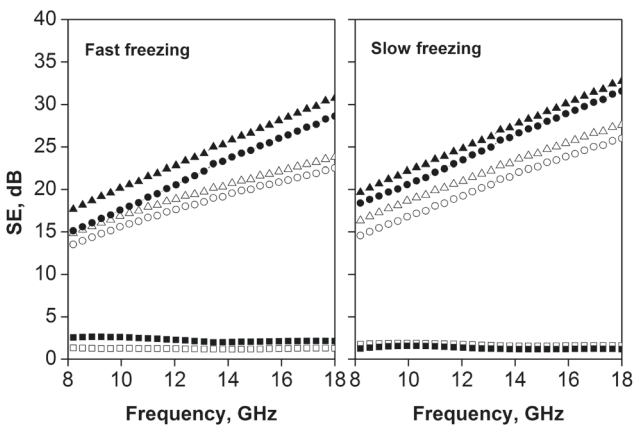

Fig. 6 Electromagnetic efficiency in the frequency range of 8–18 GHz with CNT percentages of: 4% (SE_R (□), SE_A (○), SE_T (△)) and 6% (SE_R (■), SE_A (●), SE_T (▲)). Composite thickness: 5 mm.

Conclusions

We have prepared CNT scaffolds with controlled porosity changing the freezing rate of 3, 4, 6 and 7 wt% CNT aqueous dispersions, with chitosan as the binder, and a subsequent lyophilisation step. Fast freezing in liquid nitrogen and slow freezing at −20 °C were used. For machining to the geometry required for the characterization scaffolds were infiltrated with an epoxy resin.

Characterization by mercury porosimetry showed an irregular pore size which depends on the freezing rate: close to 20 microns for fast freezing and 100–150 microns for slowly frozen samples. The composites show high conductivity values with low CNT loading (10 to 17 S m^{-1}) confirming that pore walls form a percolated network beyond the percolation threshold.

Power analysis has revealed particularly low transmitted power, not exceeding in any case 10% of incident power. Additionally, the absorbed power was significantly greater (close to 70%) than the reflected power (close to 30%). More interestingly, samples with the highest pore size and porosity presented the lowest reflected power and the highest absorbed power, which allows considering them as electromagnetic radiation absorbing materials.

These results suggest that controlling the fraction, size, shape and distribution may open the possibility of modulating the phenomenon of reflection of electromagnetic radiation.

Acknowledgements

This work was supported by grants NANOARQ (MAT2014-57557-R) from the Spanish Ministerio de Ciencia y Tecnología.

Notes and references

1 A. N. Yussof, M. H. Abdullah, S. H. Ahmad, S. F. Jusoh, A. A. Mansor and S. A. A. Hamid, *J. Appl. Phys.*, 2002, **92**, 876–882.
2 S. Biswas, G. P. Kar and S. Bose, *Nanoscale*, 2015, **7**, 11334–11351.
3 K. Singh, A. Ohlan, V. H. Pham, R. Balasubramaniyan, S. Varshney, J. Jang, S. H. Hur, W. M. Choi, M. Kumar, S. K. Dhawan, B. S. Kong and J. S. Chung, *Nanoscale*, 2013, **5**, 2411.
4 B. J. Madhu, S. T. Ashwini, B. Shruthi, B. S. Divyashree, A. Manjunath and H. S. Jayanna, *Mater. Sci. Eng., B*, 2014, **186**, 1–6.
5 P. Verma, P. Saini, R. S. Malik and V. Choudhary, *Carbon*, 2015, **89**, 308–317.
6 D. D. L. Chung, *Carbon*, 2001, **39**, 279–285.
7 K. H. Gonschorek and R. Vick, *Electromagnetic Compatibility for Device Design and System Integration, Chap. 17: Skin Effect and Shielding Theory of Schelkunoff*, Springer, Berlin, Heidelberg, 2009, pp. 377–392.
8 M. H. Al-Saleh and U. Sundararaj, *Carbon*, 2009, **47**, 1738–1746.
9 M. H. Al-Saleh, W. H. Sadaah and U. Sundararaj, *Carbon*, 2013, **60**, 146–156.
10 M. Crespo, M. González, A. L. Elías, L. P. Rajukumar, J. Baselga, M. Terrones and J. Pozuelo, *Phys. Status Solidi RRL*, 2014, **8**, 698–704.
11 M. H. Al-Saleh and U. Sundararaj, *J. Phys. D: Appl. Phys.*, 2013, **46**, 035304–035310.
12 N. Zhao, T. Zou, C. Shi, J. Li and W. Guo, *Mater. Sci. Eng., B*, 2006, **127**, 207–211.
13 X. C. Tong, *Advanced Materials and Design for Electromagnetic Interference Shielding*, Francis & Taylor, Boca Raton, FL, USA, 2009.
14 H. M. Kim, K. Kim, C. Y. Lee, J. Joo, S. J. Cho, H. S. Yoon, D. A. Pejakovic, J. W. Yoo and A. J. Epstein, *Appl. Phys. Lett.*, 2004, **84**, 589–591.
15 J. M. Thomassin, C. Jérôme, T. Pardoen, C. Bailly, I. Huynen and C. Detrembleur, *Mater. Sci. Eng., R*, 2013, **74**, 211–232.
16 M. Crespo, N. Méndez, M. González, J. Baselga and J. Pozuelo, *Carbon*, 2014, **74**, 63–72.
17 B. Wen, X. X. Wang, W. Q. Cao, H. L. Shi, M. M. Lu, G. Wang, H. B. Jin, W. Z. Wang, J. Yuan and M. S. Cao, *Nanoscale*, 2014, **6**, 5754–5761.
18 T. K. Gupta, B. P. Singh, R. B. Mathur and S. R. Dhakate, *Nanoscale*, 2014, **5**, 842–851.
19 M. T. Chen, L. Zhang, S. S. Duan, S. L. Jing, H. Jiang, M. L. Luo and C. Z. Li, *Nanoscale*, 2014, **6**, 3796–3803.
20 Y. Huang, N. Li, Y. Ma, F. Du, F. Li, X. He, X. Lin, H. Gao and Y. Chen, *Carbon*, 2007, **45**, 1614–1621.
21 A. P. Singh, M. Mishra, D. P. Hashim, T. N. Narayanan, M. G. Hahm, P. Kumar, J. Dwivedi, G. Kedawat, A. Gupta, B. P. Singh, A. Chandra, R. Vajtai, S. K. Dhawan, P. M. Ajayan and B. K. Gupta, *Carbon*, 2015, **85**, 79–88.
22 W. L. Song, M. S. Cao, M. M. Lu, S. Bi, C. Y. Wang, J. Liu, J. Yuan and L. Z. Fan, *Carbon*, 2014, **66**, 67–76.
23 J. Liang, Y. Wang, Y. Huang, Y. Ma, Z. Liu, J. Cai, C. Zhang, H. Gao and Y. Chen, *Carbon*, 2009, **47**, 922–925.
24 C. Wang, X. Han, P. Xu, X. Zhang, X. Y. Du, S. Hu, J. Wang and X. Wang, *Appl. Phys. Lett.*, 2011, **98**, 072906.
25 S. K. Hong, K. Y. Kim, T. Y. Kim, J. H. Kim, S. W. Park, J. H. Kim and B. J. Cho, *Nanotechnology*, 2012, **23**, 455704.
26 N. Li, Y. Huang, F. Du, X. He, X. Lin, H. Gao, Y. Ma, F. Li, Y. Chen and P. C. Eklund, *Nano Lett.*, 2006, **6**, 1141–1145.
27 M. Inagaki, *New Carbon Mater.*, 2009, **24**, 193–232.
28 K. A. Wepasnick, B. A. Smith, K. E. Schrote, H. K. Wilson, S. R. Diegelmann and D. H. Fairbrother, *Carbon*, 2011, **49**, 24–36.
29 Y. Peng and H. Liu, *Ind. Eng. Chem. Res.*, 2006, **45**, 6483–6488.
30 V. Datsyuk, M. Kalyva, K. Papagelis, J. Prthenios, D. Tasis, A. Siokou, I. Kallitsis and C. Galiotis, *Carbon*, 2008, **46**, 833–840.
31 N. V. Qui, P. Scholz, T. Krech, T. F. Keller, K. Pollok and B. Ondruschka, *Catal. Commun.*, 2011, **12**, 464–469.
32 O. Martín, H. R. Gutierrez, A. Maroto-ValientE, M. Terrones, T. Blanco and J. Baselga, *Mater. Chem. Phys.*, 2013, **140**, 499–504.
33 M. S. Cao, W. L. Song, Z. L. Hou, B. Wen and J. Yuang, *Carbon*, 2010, **48**, 788–796.
34 *Agilent 85071E Materials Measurement Software*.
35 H. Giesche, *Syst. Charact.*, 2006, **23**, 1–11.
36 A. Ameli, M. Nofar, C. B. Park, P. Pötschke and G. Rizvi, *Carbon*, 2014, **71**, 206–217.
37 C. A. Grimes, C. Mungle, D. Kouzoudis, S. Fang and P. C. Eklund, *Chem. Phys. Lett.*, 2000, **319**, 460–464.
38 Q. Liu, D. Zhang and T. Fan, *Appl. Phys. Lett.*, 2008, **93**, 013110.
39 L. W. Hrubesh, L. E. Keene and V. R. Latorre, *J. Mater. Res.*, 1993, **8**, 1736–1741.
40 X. Xiao, R. Streiter, G. Ruan, R. Song, T. Otto and T. Gessner, *Microelectron. Eng.*, 2000, **54**, 295–301.
41 F. Moglie, D. Micheli, S. Laurenzi, M. Marchetti and V. Mariani Primiani, *Carbon*, 2012, **50**, 1972–1980.